Journal of Nuclear Materials 384 (2009) 30–37

Contents lists available at ScienceDirect

Journal of Nuclear Materials

journal homepage: www.elsevier.com/locate/jnucmat

Annealing of cold worked two-phase Zr-2.5 Nb—Associated microstructural developments

V.D. Hiwarkar [a], S.K. Sahoo [a], I. Samajdar [a,*], K. Narasimhan [a], K.V. Mani Krishna [b], G.K. Dey [b], D. Srivastava [b], R. Tewari [b], S. Banerjee [b]

[a] Department of Metallurgical Engineering and Materials Science, IIT Bombay, Powai, Mumbai-400 076, Maharashtra, India
[b] Materials Science Division, Bhabha Atomic Research Center, Mumbai, India

ARTICLE INFO

Article history:
Received 10 April 2008
Accepted 2 October 2008

ABSTRACT

Pilgered two-phase Zr-2.5 Nb was subjected to recovery (400 °C) and recrystallization (700 °C) annealing – broad objective was to bring out associated microstructural developments. Effects of recovery and recrystallization were indexed in terms of changes in hardness, lattice strain, stored energy of cold work and residual stress. Though recovery did not cause significant changes in grain/phase structure; visible coarsening of 2nd phase was associated with recrystallization. Such coarsening continued even after the completion of primary recrystallization, with concurrent and noticeable changes in microstructure and in crystallographic texture.

1. Introduction

Zirconium (Zr) alloys, both single and two-phase, are widely used for structural applications in the nuclear industry [1,2]. Two-phase Zr-2.5 Nb is a typical example – material of choice for pressure tubes in PHWRs (pressurized heavy water reactor) [1,3]. The microstructure of a finished pressure tube [4] consists of grains, of primary hexagonal phase, in cold worked but stress-relieved state with nearly continuous 'filaments' of 2nd phase (10–15%, by area) bcc β. Final annealing may alter/affect [4] the aforementioned microstructure. Zr microstructure, including crystallographic texture [1,4–10] and stress state [1,11,12], determines relevant properties [1,13–30]. This, on the other hand, provides the basis for fine-tuning the processing stages [1,18,31].

The typical processing of Zr-2.5 Nb pressure tube consists [1,4,31–34] of hot extrusion followed by a series of cold working with intermediate annealing (Fig. 1). The cold working steps are implemented through tube-drawing or pilgering/plug-rolling. The later is a process of simultaneous reduction in tube diameter and in wall thickness – a compression forming process normally attributed to have excellent formability and superior control of texture and microstructure [1]. The cold working is followed by annealing, aimed at recovery and/or recrystallization of the cold worked structure [4].

Annealing, both recovery and recrystallization, is a subject of considerable scientific and industrial importance. This can be easily appreciated by looking at some of the text-books [1,35,36] and review articles [37,38]. The impressive range of literature on the subject is, however, concentrated mostly on annealing of single-phase metallic materials – including alloys containing hard non-shearable particles. Studies on annealing in common two-phase (with shearable or semi-shearable 2nd phase) alloys are less frequent [39–43]; while such studies in two-phase Zr alloys are rare [44,45]. This was the motivation behind the present study.

Hot extruded Zr-2.5 Nb was subjected to pilgering (see Fig. 1) – approximately 58% reduction in wall thickness was provided.[1] This was then subjected to annealing treatments at 400 and 700 °C, aimed, respectively, at causing recovery and recrystallization. The microstructural developments were monitored through a combination of microhardness, X-ray diffraction (for crystallographic texture, stored energy of cold work and residual stress) and electron diffraction (electron backscattered diffraction or EBSD) studies. The aim was to bring out annealing associated microstructural developments in two-phase Zr-2.5 Nb.

2. Experimental methods

Pilgered Zr-2.5 Nb, chemical composition listed in Table 1, was obtained from the fabrication sequence of pressure tube [1,4,31,32]. Hot extruded alloy was subjected to cold pilgering – approximately 58% reduction in wall thickness (see Fig. 1). Samples were annealed in a salt bath for 400 and 700 °C. Different annealing times were used and samples were water quenched after the isothermal treatments. To monitor extent of softening, microhardness readings (at least seven readings per sample) were taken at 500 g load. For subsequent characterizations, both X-ray and

* Corresponding author. Tel.: +91 2225767621; fax: +91 2225723480.
E-mail address: indra@iitb.ac.in (I. Samajdar).

[1] Zr-2.5 Nb was obtained after the so-called first pilgering operation in a typical fabrication schedule [1,4].

0022-3115/$ - see front matter © 2008 Elsevier B.V. All rights reserved.
doi:10.1016/j.jnucmat.2008.10.006

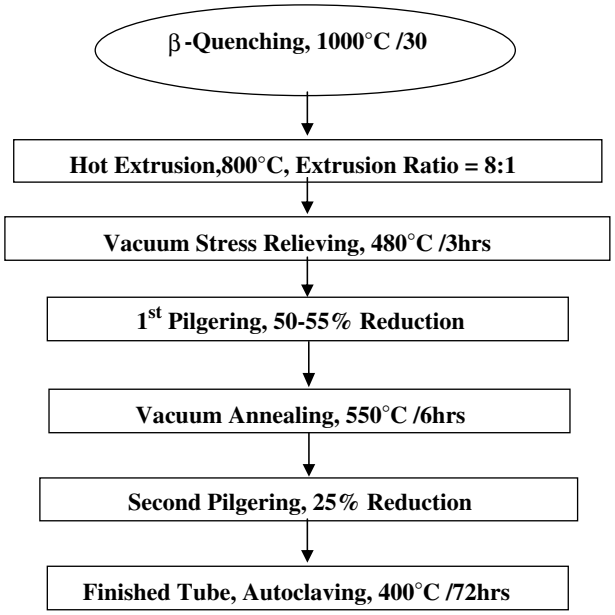

Fig. 1. Flow sheet for the fabrication of Zr-2.5 wt% Nb pressure tube by the modified/Indian route [1,4,31].

Table 1
Chemical composition of Zr-2.5 Nb used in the present study.

Niobium (wt%)	Oxygen (ppm)	Iron (ppm)	Hydrogen (ppm)	Nitrogen (ppm)
2.51	1092	1250	<10	30

electron diffraction, the samples were electropolished by using an electrolyte of 80:20 methyl alcohol and perchloric acid under 21 V at −40 °C. Limited TEM studies were carried out in a Jeol 3010 microscope operated at 300 keV.

2.1. X-ray diffraction (XRD)

Electropolished samples, mid-thickness section of the rolling (containing rolling and transverse directions) plane, were used for XRD measurements in a Panalytical MRD system. High resolution (0.02° step size) $\theta-2\theta$ (where θ is the Bragg angle) scans were used for lattice strain and stored energy estimations. Lattice strains were estimated from the slopes of $\sin\theta$ vs. $B\cos\theta$ – the classical Williamson–Hall plots [46–48]; where

$$B^2 = B_r^2 - B_a^2, \tag{1}$$

B_r and B_a are the measured values of FWHM (full width half maximum) respective for reference and standard samples. Fully annealed/recrystallized material was taken as the standard sample. It may be noted that the slope of a Williamson–Hall plot gives lattice microstrains and the intercept (on y-axis) indicates domain size [46–48]. The present study uses Williamson–Hall plots [46–48], which are indeed rigorous analysis, to estimate the lattice microstrain values. The slope of Williamson–Hall plots, $B/\tan\theta$, provides the lattice strain. The estimation of the linear fit, as used in Williamson–Hall, is converted into error-bars and used in the subsequent figures representing lattice strain estimates.

Stored energy values, for the respective poles, were estimated using Stibitz formula [49,50]

$$\bar{E}_j(\alpha,\beta) = \frac{3}{2} Y_{hkl} \frac{(\Delta d/d)^2}{(1+2\nu_{hkl}^2)}, \tag{2}$$

Table 2
Young's modulus and Poisson's ratio for different poles [51]. These values were used in the Stibitz formula, Eq. (2), to estimate stored energies for respective poles.

Pole (hkil)	Y (in GPa)	ν
$(01\bar{1}1)$	90.1	0.34
$(11\bar{2}0)$	99.01	0.32
$(02\bar{2}1)$	95.24	0.32
$(11\bar{2}2)$	97.6	0.33
$(12\bar{3}1)$	96.7	0.32
$(11\bar{2}4)$	92.5	0.34
$(01\bar{1}5)$	109.5	0.32

where $\bar{E}_j(\alpha,\beta)$ is the stored energy and Y_{hkl} and ν_{hkl} are Young's modulus and Poisson's ratio. Table 2 lists the values of Y_{hkl} and ν_{hkl} for respective poles [51], as used in the present study. $\frac{\Delta d}{d}$ was obtained from the peak profiles as

$$\frac{\Delta d}{d} = \frac{B}{2\tan\theta}. \tag{3}$$

The residual stresses were estimated by Reusse's model (standard $\sin^2\psi$ method) for different poles [1,52]. The same poles, (0002), $(01\bar{1}2)$, $(01\bar{1}3)$ and $(11\bar{2}0)$, were also taken for bulk texture measurements. Subsequent ODF (orientation distribution function) analyses were made through a commercial program LaboTex [53]. For three-dimensional (3D) ODF plots, slicer–dicer (a commercial graphics program) was used/adopted.

2.2. Electron backscattered diffraction (EBSD)

Fei Quanta-200HV SEM (scanning electron microscope) using a TSL-OIM EBSD package was used for the EBSD measurements. At least four scans, and a total area of 1 mm × 2 mm, were taken from each sample at 0.1 μm step size. EBSD parameters, beam as well as video, were identical between the scans. The accuracy of automated indexing is judged by the so-called confidence index (CI). Where

$$\mathrm{CI} = \frac{(V_{\mathrm{First}} - V_{\mathrm{Second}})}{V_{\mathrm{Total}}}. \tag{4}$$

From the detected bands multiple solutions may exist. Each solution gets certain number of 'votes'. V_{First} and V_{Second} respectively, represent solutions with first and second highest votes, while V_{Total} is the total number of votes from all possible solutions. A low CI does not necessarily mean incorrect indexing, but may represent measurement points of *questionable reliability*.

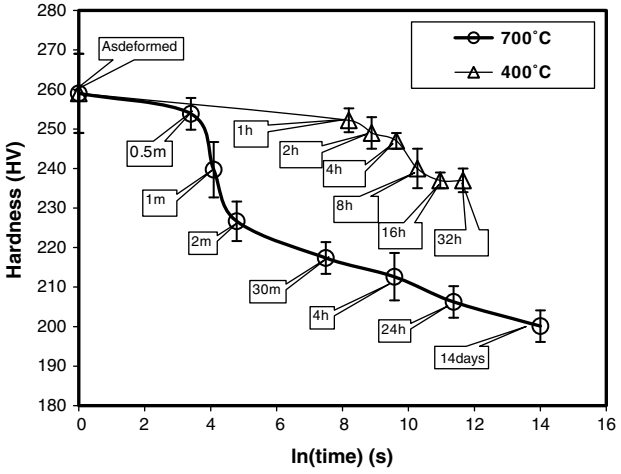

Fig. 2. Hardness vs. ln(annealing time) for 400 and 700 °C annealing.

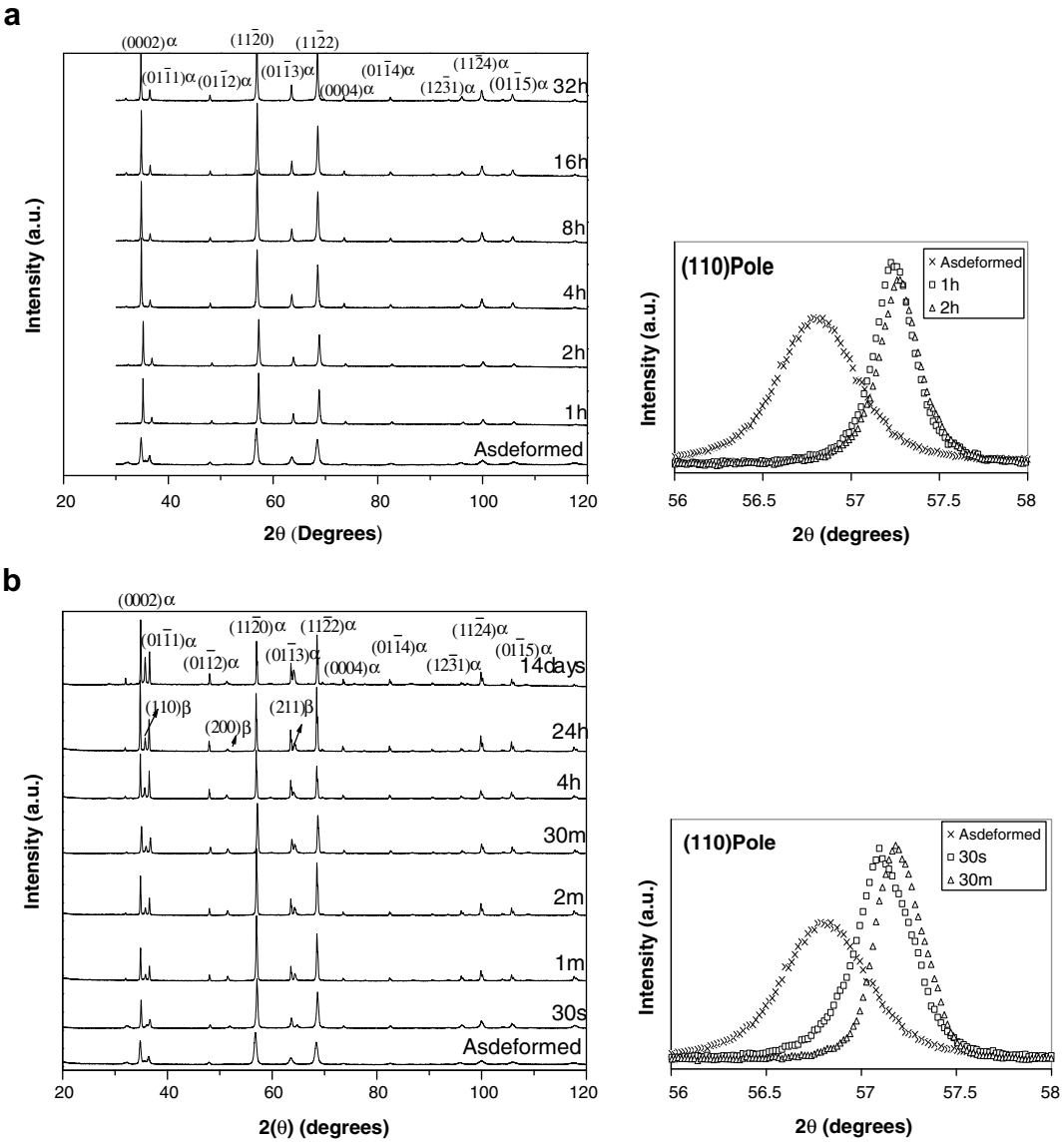

Fig. 3. XRD scans of intensity vs. 2θ for different annealing times after (a) 400 °C and (b) 700 °C annealing. The positions of the α (hcp primary phase) and β (bcc 2nd phase) peaks are indicated. The relative peak broadening and peak shift of $(1\,1\,\bar{2}\,0)$ pole is shown for selected annealing times.

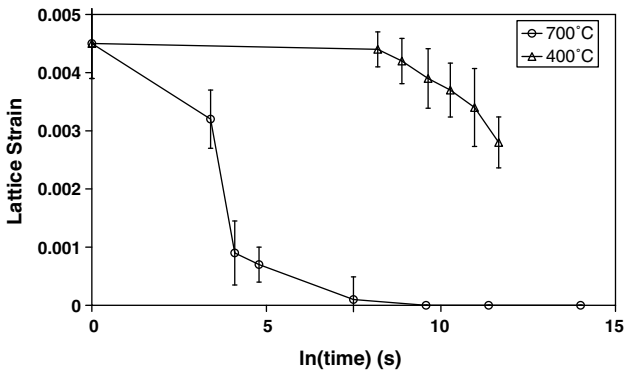

Fig. 4. Lattice strain (from Williamson–Hall [46–48] plots) vs. annealing times after 400 and 700 °C annealing.

For EBSD analyses, grain definition is critical. Grains were identified from continuous presence of more than 15° boundary. From such grains (of both phases), average grain size, grain average misorientation (GAM) and grain orientation spread (GOS) values were estimated. GOS represents average deviation between measurement points, in a grain, and the average grain orientation. GAM, on the other hand, provides average misorientation between neighboring measurement points in a grain.

3. Results

Fig. 2 summarizes the results on microhardness for the respective annealing treatments. The figure formed the basis for subsequent structural characterizations. These were in terms of X-ray (XRD) and electron (EBSD) diffraction and the output of the two techniques are presented separately.

3.1. X-ray diffraction (XRD)

Fig. 3 shows the entire band of 2θ scans for the 400 and 700 °C treatments. The observations can be summarized as:

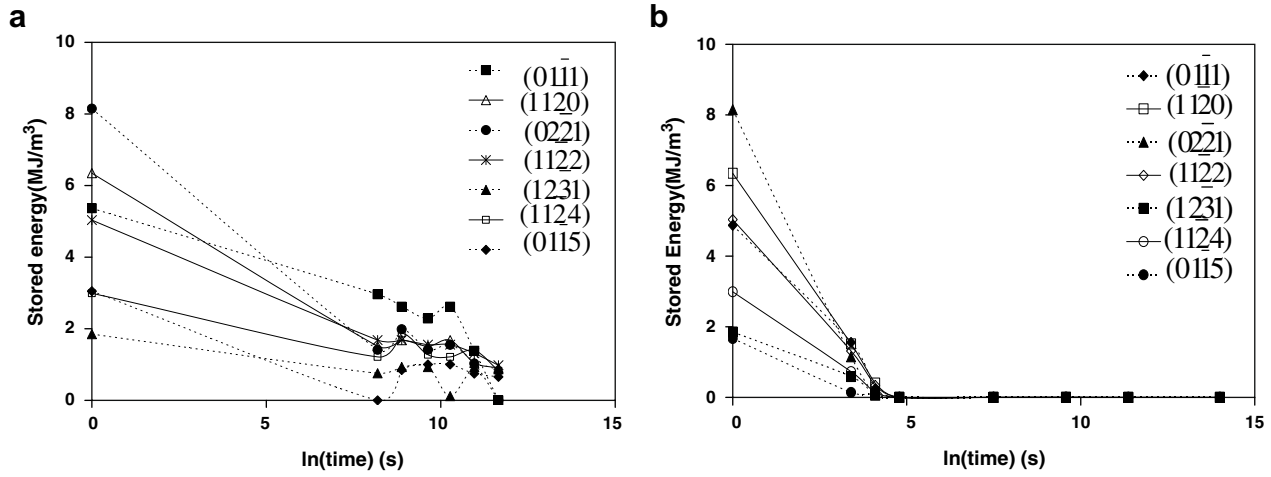

Fig. 5. Stored energy (in Mega J/m^3–MJ/m^3) vs. ln(time) for (a) 400 °C and (b) 700 °C annealing. Stored energy estimations were obtained from XRD data using standard Stibitz's (Eq. (2)) formulation.

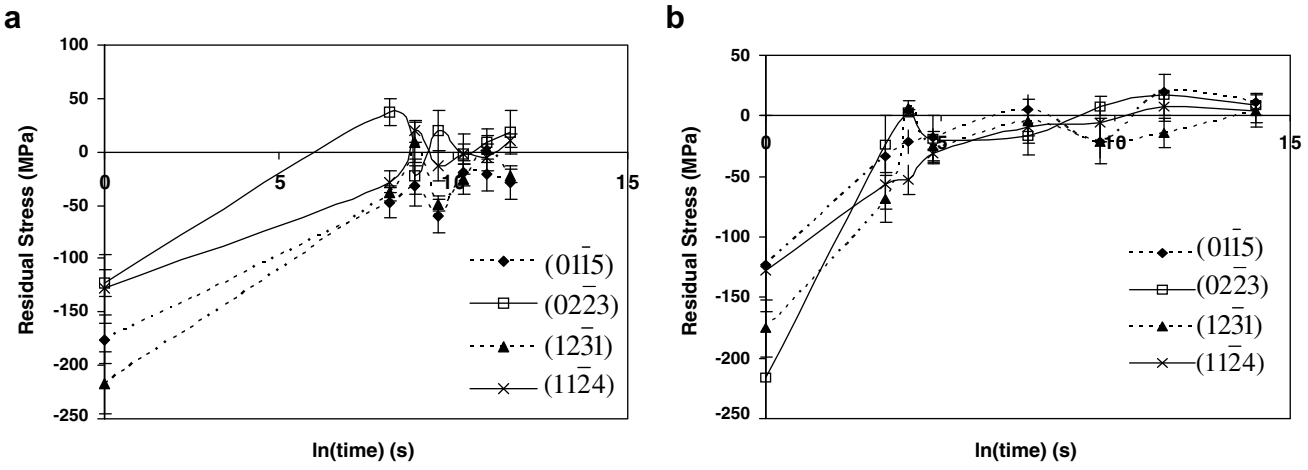

Fig. 6. Residual Stress vs. ln(time) for (a) 400 °C and (b) 700 °C annealing. Residual stresses were measured standard by sin$^2\psi$ (XRD) method [1,52].

- *400 °C annealing:* Peaks for 2nd phase β were insignificant. Though the ratios of peak intensities[2] did not change substantially, there were significant changes in peak widths and peak position(s).
- *700 °C annealing:* β peaks were increasingly visible – especially after prolonged annealing. Longer annealing periods were also associated with significant modifications in peak intensity ratios. Shorter annealing times, on the other hand, brought noticeable changes in peak positions and peak widths.

It needs to be pointed out that peak intensity ratios is a crude measure of bulk crystallographic texture, while the peak width and position can be taken as indicators of lattice strain (or stored energy of cold work) and residual stress, respectively.

Fig. 4 shows the XRD estimated lattice strains for the 400 and 700 °C annealing. A combination of Figs. 2 and 4 do provide a hint of softening kinetics. The softening can also be viewed in terms of changes in stored energy of cold work, see Fig. 5, and of residual stress, see Fig. 6. Though the starting pilgered material had anisotropic[3] stored energy and residual stress, such anisotropy dropped with progress in annealing. The values were insignificant beyond 30 s annealing at 700 °C, while 400 °C annealing (1 h and more) led to elimination of residual stresses though stored energy of cold work remained within measurement limits.

As in Fig. 7, bulk textures were plotted as 3D ODFs.[4] It is important to point out, at this stage, that significant improvement in our understanding of crystallographic texture came through extension of pole-figure data into 3D Euler space – i.e., from pole-figures to ODFs. ODFs were traditionally represented [1,4,6–8,30] in 2D Euler space, mainly due to non-availability of suitable/potent graphics tools. Today, the availability of excellent graphics and possibility of interface programs (user written/defined) to utilize such graphics exist. The result is 3D ODFs – as used in the present study and also in earlier studies of the same research group [10]. A 3D ODF, as in Fig. 7, plots the ODF intensities ($f(g)$) [1,7] in 3D Euler space.

As shown in Fig. 7(a), the pilgered texture is a generalized <10$\bar{1}$0> type [6,10] of fiber texture. This texture did not change by 400 °C annealing – an expected trend considering that recovery cannot affect bulk crystallographic texture [1,35]. It is, however, important to note that till 30 min annealing at 700 °C, the bulk

[2] Between major peaks.
[3] Significantly different values between different (hkil) poles.
[4] Common $f(g)$ scale for the 3D ODFs is included in the figure.

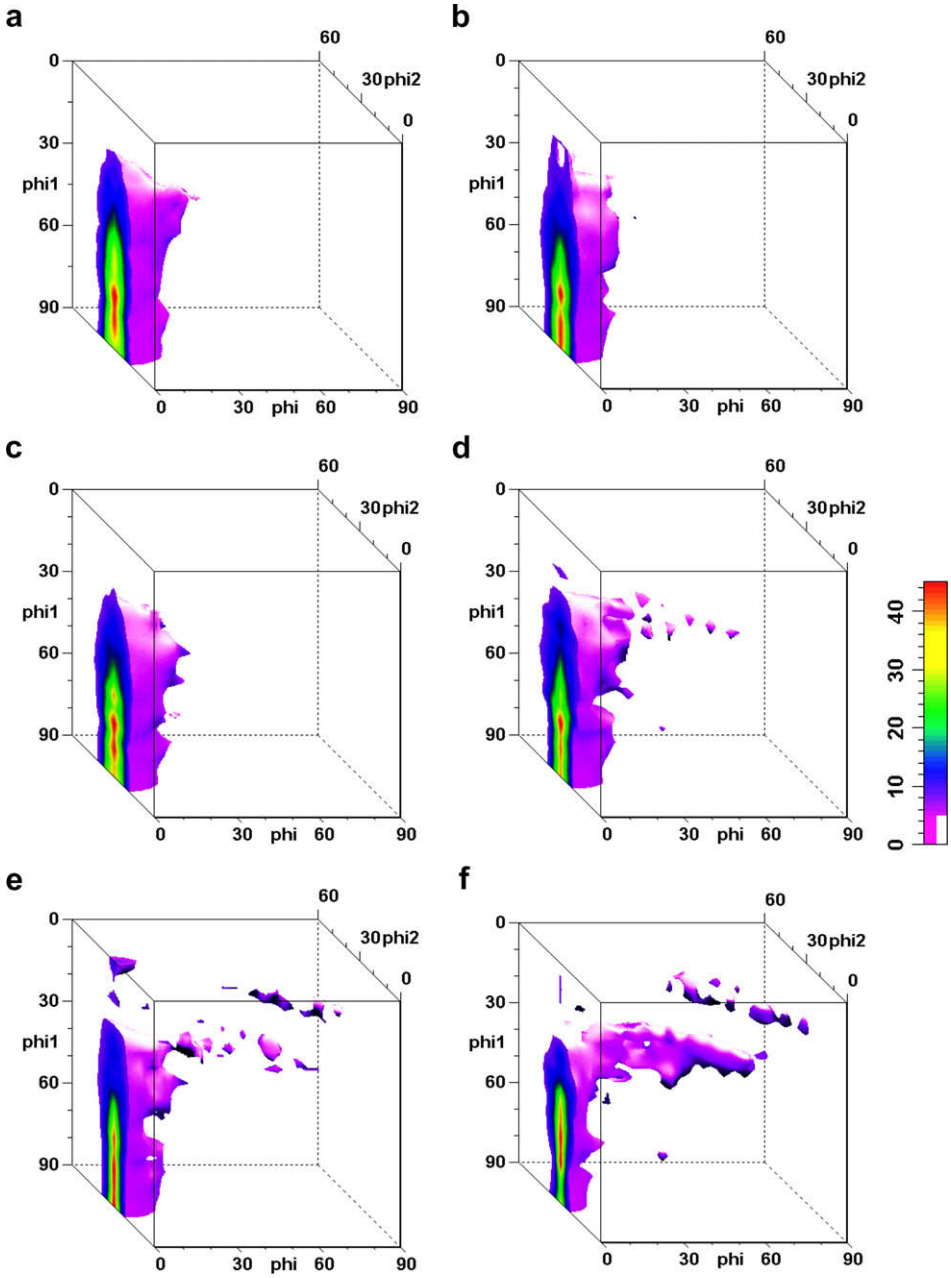

Fig. 7. Three-dimensional (3D) ODFs (orientation distribution function) for (a) pilgered sample and the same after 700 °C annealing for (b) 1 min (c) 2 min (d) 30 min (e) 4 h (f) 14 days. Axes are in Phi1, Phi and Phi2 – Euler angles in Bunge notation [1,7].

crystallographic texture did not change. This is possibly one of the most significant results of the present study. ODFs were nearly identical up to 30 min annealing at 700 °C, Fig. 7(a–c), or the same <10$\bar{1}$0> fiber remained with nearly identical strength and intensity distributions. Only beyond 30 min, elements of (0001) basal texture emerged. Significant basal fiber was observed only after 14 days annealing at 700 °C.

3.2. Electron backscattered diffraction (EBSD)

The pilgered sample was not amenable to EBSD measurements in a thermionic emission (W-filament) SEM. 400 °C Annealing, irrespective of the time periods, did not change this situation. Annealing at 700 °C and for 30 s, on the other hand, brought clearly identifiable α (hexagonal primary phase) and fine 2nd phase β against a backdrop of measurement points of questionable reliability (low confidence index points) – Fig. 8(a). Further annealing (Fig. 8(b)) led to equiaxed α grains and coarsening of β. After the highest annealing period used in the present study (Fig. 8(c) – 14 days annealing at 700 °C), 2nd phase β was observed at some select tri-junctions of the α grains.

Fig. 9 brings out further information from the EBSD measurements. The in-grain misorientations, both GOS and GAM, dropped with annealing time – stagnated at and above 2 min, see Fig. 9(a) and (b). It needs to be noted that the stagnated GOS/GAM values fall within measurement uncertainty – i.e., comparable to values estimated for annealed/recrystallized single crystals. Other than an initial increase in α grain size, the grain sizes of both phases showed (Fig. 9(c) and (d)) a rapid growth for annealing periods of 4 h and beyond.

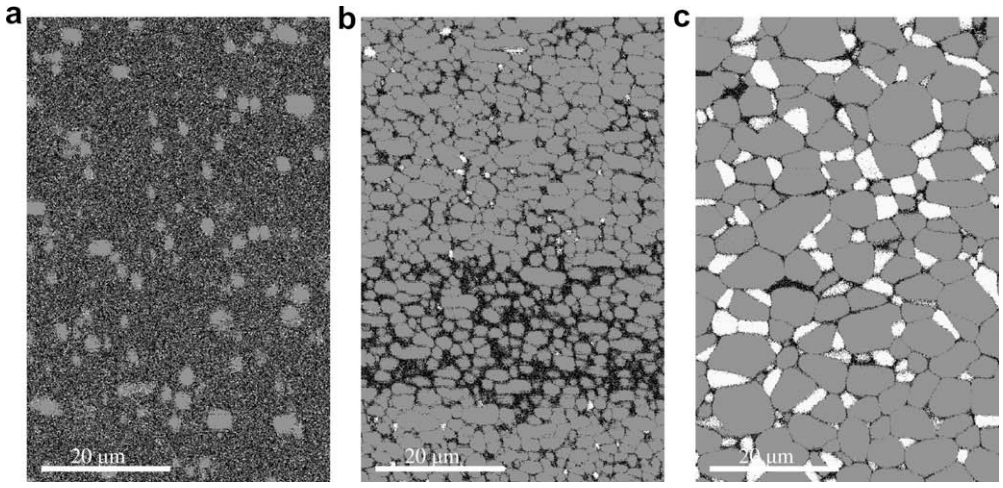

Fig. 8. EBSD images after 700 °C annealing for (a) 30 s, (b) 4 h and (c) 14 days. Hexagonal primary phase and the bcc 2nd phase are marked as light grey and white, respectively. Measurement points with questionable reliability (the so-called low, below 0.05, confidence index) are shown in black.

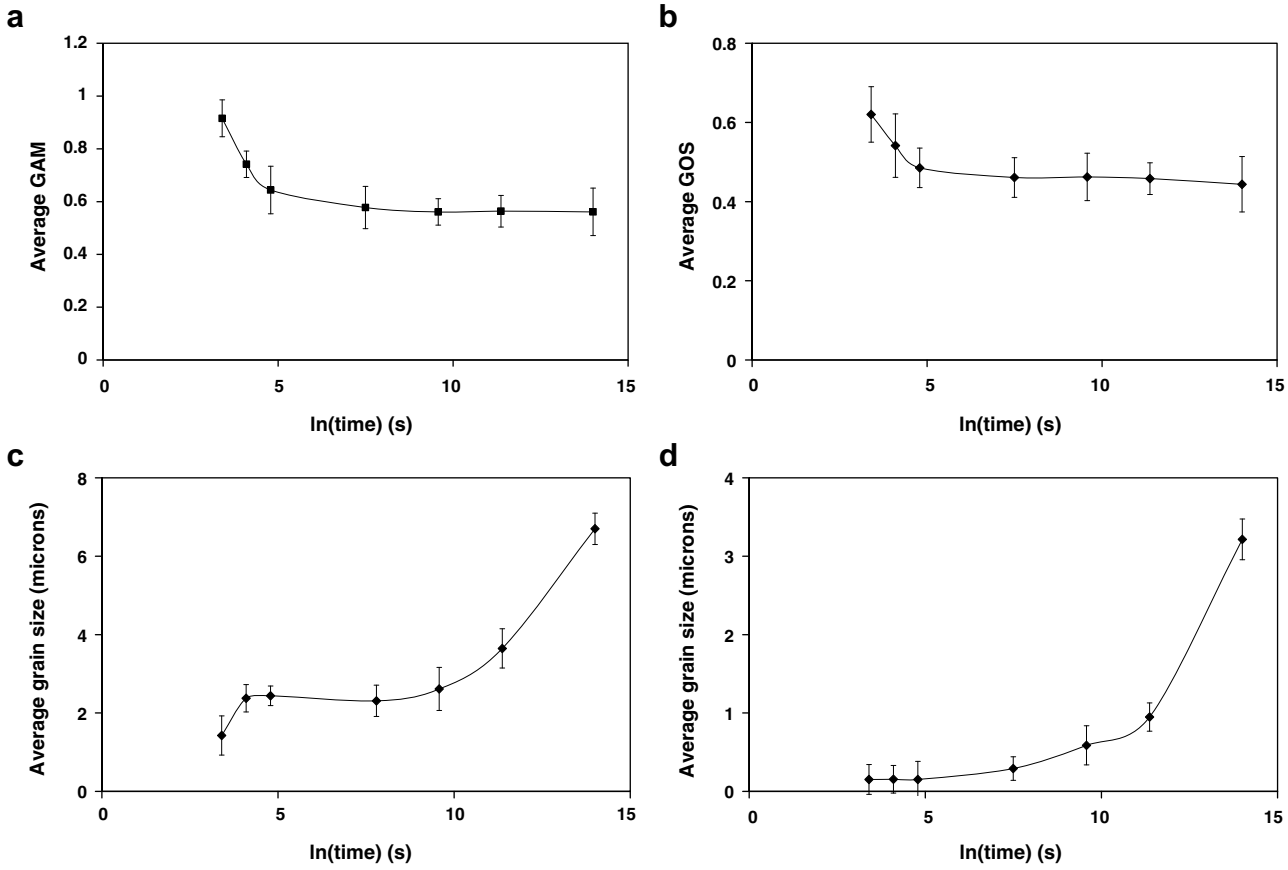

Fig. 9. EBSD estimated (a) average GAM and (b) average GOS for primary hexagonal α phase. (c) Average α (hcp matrix phase) grain size and (d) average β (bcc 2nd phase) grain size. The values are plotted with respect to ln(time) for 700 °C annealing. Standard deviation values, based on data from several scans, are also shown.

4. Discussion

The present study deals with annealing of cold worked (58% cold pilgered) two-phase Zr-2.5 Nb. Two annealing temperatures were selected. 400 °C annealing is expected to cause recovery with or without noticeable aging response [54–57]; while 700 °C annealing would lead to a combination of primary recrystallization and grain coarsening. The extent of annealing or softening was brought out through a variety of measurement techniques – microhardness, XRD estimated lattice strain and stored energy and residual stress, microtextures through EBSD. Such estimates have different resolution and applicability. For example, EBSD measurements were valid only for 700 °C annealing; while softening[5] estimates through microhardness and lattice strain had relatively poor resolution at higher degree of softening. It needs to be

[5] For both recovery and recrystallization.

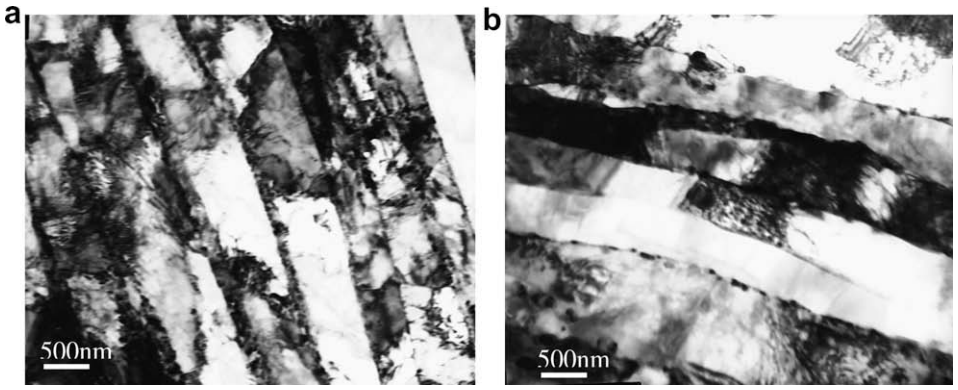

Fig. 10. TEM images of (a) pilgered and (b) 700 °C–30 s annealed samples.

noted that the prior deformation structure (e.g., hot extruded structure – in case of the present study) may greatly influence the annealing behavior. A classic example is reference [54], where differences in prior thermal treatments[6] produced significantly different results. For example, reference [54] reported an aging response, an increase in yield strength, at 400 °C. Such an aging response was not observed in the present study.

4.1. Recovery

Pligered microstructure contains sub-micron α grains and very fine 2nd phase β lamella [4] – see Fig. 10(a). It needs to be noted that there are limits to the EBSD technique because of grain size and dislocation density. The EBSD technique can only produce meaningful results, when there has been sufficient recovery and/or grain coarsening leading to measurable diffraction patterns. The recovery treatments used in the present study did not bring out indexable Kikuchi patterns.

The interesting observations on recovery are the patterns of recovery kinetics and possible orientation sensitivity of stored energy and residual stress. Recovery kinetics in single-phase metallic materials is reported [1,37] to obey either linear or logarithmic relationship(s). The recovery kinetics (in terms of microhardness drop) in the present two-phase alloy also appears to follow a logarithmic relationship

$$X = 4.9\ln(t) - 33.4, \tag{5}$$

where X is the extent of recovery (in the present case, change in microhardness values) and t is time (in s).

The starting structure had differences in stored energy and in residual stress between the respective poles. With the smallest recovery period[7] used in the present study (1 h at 400 °C), such differences appeared to become insignificant – see Figs. 5(b) and 6(b). It remains to be established how such response compares with single-phase Zr; though it is perhaps safe to state that in Zr-2.5 Nb a minimum (as detectable by hardness response) recovery treatment at 400 °C is sufficient to cause effective stress relieving.

4.2. Recrystallization and grain coarsening

It is important to pin-point the completion of primary recrystallization. Lattice strain estimates (Fig. 4) beyond 1 min annealing were insignificant, while microhardness values (Fig. 2) were also biased by grain coarsening. EBSD, especially in terms of in-grain misorientation – Fig. 9(a) and (b), appears to provide an easy solution. GOS and GAM stagnated at and above 2 min annealing. This and visual observation of EBSD structures led to the conclusion that the primary recrystallization was over by 2 min annealing at 700 °C. What followed subsequently was grain coarsening – Figs. 8 and 9(c) and (d).

Two-phase Zr shows an interesting response during cold deformation [4,6]. The majority α phase does not go through significant texture developments, as the strain is effectively partitioned to 2nd phase β. The continuity of β appears to be a key factor for such 'texture retention' [4,6]. The present study shows, conclusively and for the first time, that primary recrystallization in such two-phase alloy also does not change the texture. For possible explanation, one needs to visualize the deformed structure – see Fig. 10(a). Deformed α regions/bands were typically outlined by fine β lamellas. Though in Fig. 10(a) presence of strong contrasts from orientations and dislocations make a clear visualization difficult, it is understood/reported [4] that except for occasional discontinuities the β lamellas are nearly continuous. Subsequent recovery/early-recrystallization spherodized the β, Fig. 10(b), and such spherodized β outlined the α–α band boundaries. This, in turn, restricts the recrystallized grains from growing into a neighboring band. Even if nucleation is 'delayed' in some bands, they all would eventually present recrystallized α grains. Unlike a typical single-phase system, regions/orientation with delayed/non-preferred nucleation does not get consumed and eventually all bands contribute to the final recrystallization texture. This appears to be a plausible hypothesis explaining the absence of recrystallization texture developments in the present Zr-2.5 Nb. To validate (quantitatively and objectively – though subjective validation, as Fig. 9, is always possible) such a hypothesis through direct microscopic observations (especially EBSD – TEM provides a more restricted field of view) is difficult, though the subsequent coarsening response offers an indirect support. As the annealing continued, 2nd phase β visibly coarsened (Figs. 8 and 9(d)). This allowed competitive grain growth of α and concurrent texture developments (Fig. 7).

5. Conclusions

- *Recovery though 400 °C annealing*: Logarithmic recovery kinetics was observed. Minimum recovery period (1 h – when clear drop in hardness was noted) appeared to be sufficient for effective stress relief.
- *Recrystallization and grain growth through 700 °C annealing*: Primary recrystallization did not change crystallographic texture. Subsequent coarsening of 2nd phase β led to competitive grain growth in α and these resulted in textural changes.

[6] Heat treated in α–β phase field at 760 °C and then cold rolled and annealed [54], while the present study involves cold rolling/annealing of hot extruded (at 800 °C – see Fig. 1) alloy.

[7] This was selected as even smaller time periods did not bring in clear drop in microhardness response.

- *Hypothesis on absence of recrystallization texture developments:* Presence of spherodized β at the α–α band boundaries was observed during recovery/early-recrystallization. In such a microstructure, recrystallized grains are not expected to grow into a neighboring band. This rules out, in general, elimination of the bands, including bands with lower preference for nucleation. As majority of the bands, approximating the deformation texture, contributed towards recrystallization – there were no texture developments.

Acknowledgement

Support from BRNS (Board of Research on Nuclear Science), DST (Department of Science and Technology) and IFCPAR/CEFIPRA (Indo-French Centre for the promotion of advance research) are acknowledged.

References

[1] B. Verlinden, J. Driver, I. Samajdar, R.D. Doherty, Thermo-mechanical Processing of Metallic Materials, Materials Series ISBN 978-0-08-044497-0, Elsevier, Amsterdam, 2007.
[2] O.S. Charles, Nuclear Reactor Materials, Addision-Wesley, 1967. p. 130.
[3] J.A.L. Robertson, J. Nucl. Mater. 100 (1981) 108.
[4] M. Kiran Kumar, C. Vanitha, I. Samajdar, G.K. Dey, R. Tewari, D. Srivastava, S. Banerjee, J. Nucl. Mater. 335 (2004) 48.
[5] Y. Li, R. Rogge, R.A. Holt, Mater. Sci. Eng. A 437 (2006) 10.
[6] M. Kiran Kumar, I. Samajdar, N. Venkatramani, G.K. Dey, R. Tewari, D. Srivastava, S. Banerjee, Acta Mater. 51 (2003) 625.
[7] H.J. Bunge, Texture Analysis in Materials Science – Mathematical Methods, Butterworths, London, 1982.
[8] V. Randle, O. Engler, Texture Analysis Macrotexture, Microtexture and Orientation Mapping, Gordon and Breach, Australia, 2000.
[9] R.G. Ballinger, G.E. Lucas, R.M. Pelloux, J. Nucl. Mater. 126 (1984) 53.
[10] K.V. Mani Krishna, S.K. Sahoo, I. Samajdar, S. Neogy, R. Tewari, D. Srivastava, G.K. Dey, Gaur Hari Das, N. Saibaba, S. Banerjee, J. Nucl. Mater. 383 (2008) 78.
[11] G. Choudhuri, D. Srivastava, K.R. Gurumurthy, B.K. Shah, J. Nucl. Mater. 383 (2008) 178.
[12] S.K. Sahoo, V.D. Hiwarkar, I. Samajdar, G.K. Dey, D. Srivastav, R. Tiwari, S. Banerjee, Scr. Mater. 56 (2007) 963.
[13] M. Holicky, J. Schroeder, J. Nucl. Mater. 44 (1972) 31.
[14] A.R. Causey, J. Nucl. Mater. 98 (1981) 313.
[15] E.F. Ibrahim, R.A. Holt, J. Nucl. Mater. 91 (1980) 311.
[16] R.A. Holt, N. Christodoulou, A.R. Causey, J. Nucl. Mater. 317 (2003) 256.
[17] Sung Soo Kim, Young Suk Kim, J. Nucl. Mater. 279 (2000) 286.
[18] D.K. Rodgers, C.E. Coleman, M. Griffiths, G. Bickel, J.R. Theaker, I. Muir, A.A. Bahurmuz, S.St. Lawrence, M. Resta Levi, J. Nucl. Mater. 383 (2008) 22.
[19] R.N. Singh, S. Roychowdhury, V.P. Sinha, T.K. Sinha, P.K. De, S. Banerjee, Mater. Sci. Eng. A 374 (2004) 342.
[20] E. Tenckhoff, Deformation Mechanisms, Texture and Anisotropy in Zirconium and Zircaloy, ASTM, Philadelphia, PA, 1988. p. 3.
[21] A. Akhtar, A. Teghtsoonian, Acta Metall. 19 (1971) 655.
[22] K. Linga Murty, B.L. Adams, Mater. Sci. Eng. 70 (1985) 169.
[23] M.P. Puls, San-Qiang Shi, J. Rabier, J. Nucl. Mater. 336 (2005) 73.
[24] C. Lemaignan, A.T. Motta, in: R.W. Cahn, P. Hassen, E.J. Krammer (Eds.), Material Science and Technology, vol. 10B, Part II, VCH, Weinheim, 1993, p. 1.
[25] V. Perovic, G.C. Weatherly, C.J. Simpson, Scr. Metall. 16 (1982) 409.
[26] D.O. Northwood, U. Kosasih, Int. Met. Rev. 28 (1983) 92.
[27] D. Hardie, J. Nucl. Mater. 42 (1972) 317.
[28] B. Cox, J. Nucl. Mater. 179 (1990) 249.
[29] C. Nam, J. Lin, H. Li, J.A. Szpunar, R. Holt, J. Nucl. Mater. 353 (2006) 135.
[30] K. Linga Murty, J. Ravi, Wiratmo, Nucl. Eng. Des. 156 (1995) 359.
[31] D. Srivastava, G.K. Dey, S. Banerjee, Metall. Mater. Trans. 26A (1995) 2707.
[32] C. Ganguly, in: Proceedings of the Symposium Zirconium-2002, BARC, Mumbai, 2002, p. 1.
[33] G.A. Bickel, M. Grifiths, J. Nucl. Mater. 383 (2008) 9.
[34] Zulfikar H.A. Kassam, Zhirui Wang, Mater. Sci. Eng. A 158 (1992) 185.
[35] F.J. Humphreys, M. Hatherly, Recrystallization and Related Annealing Phenomena, Elsevier Science Limited, UK, 1995.
[36] E. Hornbogen, U. Koster, Recrystallization of two-phase alloys, in: F. Haessner (Ed.), Recrystallization of Metallic Materials, Dr. Riederer-Verlag Gmbh, Stuttgart, 1978, p. 159.
[37] R.D. Dohetry, D.A. Hughes, F.J. Humphreys, J.J. Jonas, D. Juul Jensen, M.E. Kassner, W.E. King, T.R. McNelley, H.J. McQueen, A.D. Rollett, Mater. Sci. Eng. A 238 (1997) 219.
[38] Paulo Rangel Rios, Fulvio Siciliano Jr., Hugo Ricardo Zschommler Sandim, Ronald Lesley Plaut, Angelo Fernando Padilha, Mater. Res. 8 (3) (2005) 225.
[39] K. Mader, E. Hornbogen, Scr. Metall. 8 (1974) 979.
[40] A.M. Parshin, M.A. Skotnikova, Metal Sci. Heat Treat. 7 (1997) 34.
[41] Tae-Hoon Kim, Jong Hyuk Baek, Jun Hwan Kim, Byoung Kwon Choi, Yong Hwan Jeong, Chang Sun Kang, Nucl. Eng. Des. 238 (2008) 1286.
[42] Chung-Min Chang, J.G. Byrne, Mater. Sci. Eng. A 160 (1993) 91.
[43] K. Kubiak, J. Sieniawski, J. Mater. Process. Technol. 78 (1998) 117.
[44] M.T. Jovanovic, R.L. Eadie, Y. Ma, M. Anderson, S. Sagat, V. Perovic, Mater. Charact. 47 (2001) 259.
[45] R.A. Holt, J. Nucl. Mater. 59 (1976) 234.
[46] B.D. Cullity, Elements of X-ray Diffraction, 2nd Ed., Addision-Wesley Publication, 1978.
[47] C. Suryanarayana, M. Grant Norton, X-ray Diffraction – a Practical Approach, Plenum, London, 1998.
[48] G.K. Williamson, W.H. Hall, Acta Metall. 1 (1953) 22.
[49] G.R. Stibitz, Phys. Rev. 49 (1937) 862.
[50] G.R. Stibitz, Phys. Rev. 8 (1947) 147.
[51] P.D. Evenschor, W. Froeliech, V. Hauk, Z. Metallkd. 62 (1971) 38.
[52] P. Van Houtte, L. De Buyser, Acta Metall. Mater. 41 (2) (1993) 323.
[53] K. Pawlik, P. Ozga, LaboTex: The Texture Analysis Software, Göttinger Arbeiten zur Geologie und Paläontologie, SB4 1999.
[54] C.E. Ells, B.A. Cheadle, J. Nucl. Mater. 23 (1967) 257.
[55] B.A. Cheadle, C.E. Ells, Electrochem. Technol. 4 (1966) 329.
[56] Manfred P. Puls, Nucl. Eng. Des. 171 (1997) 137.
[57] R. Kishore, R.N. Singh, G.K. Dey, T.K. Sinha, J. Nucl. Mater. 187 (1992) 70.